Supplementary Information for “Pathways to dewetting in hydrophobic confinement”

Richard C. Remsing *, **Erte Xi** * , **Srivathsan Vembanur** †, **Sumit Sharma** ‡, **Pablo G. Debenedetti** ‡ , **Shekhar Garde** † , and **Amish J. Patel** *

*Department of Chemical & Biomolecular Engineering, University of Pennsylvania, Philadelphia, PA 19104, USA,†Howard P. Isermann Department of Chemical & Biological Engineering, and Center for Biotechnology and Interdisciplinary Studies, Rensselaer Polytechnic Institute, Troy, NY, 12180, USA, and ‡Department of Chemical & Biological Engineering, Princeton University, Princeton, NJ 08544, USA

Submitted to Proceedings of the National Academy of Sciences of the United States of America

Estimating “Smoothed” Derivatives of the Free Energy

To demonstrate the existence of kinks in $\Delta G(N;d)$ more clearly, we plot smoothed derivatives of $\Delta G(N;d)$ in Figure 2b of the main text. Directly computing derivatives of $\Delta G(N)$ using finite difference, for example, using $\partial \Delta G/\partial N = \Delta G(N+1) - \Delta G(N)$, results in noisy estimates due to the numerical error in $\Delta G(N)$ (Figure S1). To minimize such effects, we first smooth $\Delta G(N)$ using a rectangular window function, such that

$$\Delta G_{\mathrm{smoothed}}(N) = \frac{1}{\Delta N} \sum_{N-\Delta N/2}^{N+\Delta N/2-1} \Delta G(N) \qquad \textbf{[S1]}$$

is the smoothed free energy. Smoothed derivatives are then estimated from finite differences of such smoothed free energies,

$$\frac{\partial \Delta G}{\partial N}(N) \approx \left[\Delta G_{\mathrm{smoothed}}(N+1) - \Delta G_{\mathrm{smoothed}}(N)\right]. \qquad \textbf{[S2]}$$

Derivatives of both the unsmoothed and the smoothed (using a width of $\Delta N = 10$) free energies for select values of d are compared in Figure S1.

An analogous smoothing of the first derivative was also performed in order to obtain the second derivative of the free energy, which in turn enables us to robustly estimate N_{kink} as the location of the minimum in $\partial^2 \beta \Delta G/\partial N^2$. The error in N_{kink} was estimated using block averaging; the trajectories were divided into five blocks of 1 ns each, and N_{kink} was obtained for each of the five blocks. As an example, the second derivatives for five such blocks are shown in Figure S2 for $d = 14$ Å .

Obtaining Instantaneous Interfaces that Envelop Dewetted Regions

Here, we closely follow and build upon the approach for estimating instantaneous interfaces, originally developed by Willard and Chandler [1]. In addition to considering the coarse-grained water density, we also include a coarse-grained density arising from the plate atoms into an overall, normalized coarse-grained density at (x, y, z) as follows:

$$\tilde{\rho}_{\mathrm{total}}(x,y,z;\overline{\mathbf{R}}) = \frac{\tilde{\rho}_{\mathrm{water}}(x,y,z;\overline{\mathbf{R}})}{\rho_{\mathrm{water}}^{\mathrm{bulk}}} + \frac{\tilde{\rho}_{\mathrm{plate}}(x,y,z;\overline{\mathbf{R}})}{\rho_{\mathrm{plate}}^{\mathrm{max}}}. \qquad \textbf{[S3]}$$

Here, $\overline{\mathbf{R}}$ represents the positions of all the heavy atoms in the system in a given configuration, the coarse-grained water density is normalized by the corresponding bulk density, and the coarse-grained plate density by the maximum coarse-grained plate density that occurs at the center of the plate. Defined this way, $\tilde{\rho}_{\mathrm{total}}$ is approximately equal to unity everywhere in the liquid state and near unity at the center of the plates and in the interfacial region. Configurations containing dewetted regions (cavities) will have significantly smaller values of $\tilde{\rho}_{\mathrm{total}}$ that approach zero in the vicinity of the cavity. Therefore, the $\tilde{\rho}_{\mathrm{total}} = 0.5$ iso-density surface serves as a convenient definition of the instantaneous interface, allowing us to readily visualize the position, size, and shape of the cavity; we use the Marching Cube algorithm [2] to identify the instantaneous interface. The coarse-grained density fields of the individual species are estimated using

$$\tilde{\rho}_{\alpha}(x,y,z;\overline{\mathbf{R}}) = \sum_{i=1}^{N_\alpha} \phi(x_i - x)\phi(y_i - y)\phi(z_i - z), \qquad \textbf{[S4]}$$

where α represents either the water oxygen atoms or the plate atoms, N_α is the number of atoms of type α, and (x_i, y_i, z_i) correspond to the coordinates of atom i.

For each configuration obtained from our simulations, we set up a three-dimensional grid to compute the coarse-grained density field with 0.1 nm spacing in each dimension. The coarse-graining function $\phi(x)$ is chosen to be a Gaussian with a width of 0.24 nm, which was truncated at 0.7 nm, shifted down to make it continuous, and normalized. The particular characteristics of the instantaneous interfaces thus computed, as well as those of the dewetted regions, such as their exact shapes and volumes, will depend on the choices made in Equations S3 and S4, as well as the parameters chosen. A discussion of how these choices affect the instantaneous interface calculation and which choices are judicious is beyond the scope of this work, and will be the subject of a separate publication. However, it is important to note that the qualitative insights that we obtain in this work are not sensitive to the particular choices that we make here.

Movies

The dynamical nature of the vapor tubes described in the main text can be observed in the movie shown in Movies S1 and S2. There, we show a top (Movie S1) and a side (Movie S2) view of a plate-spanning vapor tube from a simulation with a biasing potential, $\kappa(\tilde{N} - \tilde{N}^*)^2/2$; $\kappa = 0.12$ kJ/mol and $\tilde{N}^* = 650$. The average value of $\tilde{N}$ in the presence of the biasing potential was $\left\langle \tilde{N} \right\rangle = 653$. The plate atoms are shown as cyan spheres, water molecules are not shown for clarity, and the purple mesh corresponds to the instantaneous interface enveloping the vapor region. In essence, the purple mesh defines regions devoid of water molecules, such that the space outside the mesh is high in water density.

Reserved for Publication Footnotes

We show similar movies for an isolated cavity at the surface(s) of the hydrophobic plate(s) in Movies S3 and S4. The coloring scheme is the same as in Movies S1 and S2, and the configurations are taken from a biased simulation with $\tilde{N}^* = 660$ and $\kappa = 0.12$ kJ/mol; the corresponding $\left\langle \tilde{N} \right\rangle = 668$. There, an isolated cavity can be observed fluctuating in shape and size, and even moving from one plate to the other. The mechanism for bubble migration from one plate to another is an open question relevant to dewetting transitions and deserves further investigation.

Definition of the Tube and Cavity Indicator Functions

The tube indicator function $h_{\rm tube}$ is determined by examining the coarse-grained density field, $\tilde{\rho}_{\rm total}$, between the two plates. We define the x-coordinate to be perpendicular to the plates, such that the two plates are located at x_1 and x_2, respectively, with $x_1 < x_2$. We additionally define a buffer region $b = 0.4$ nm from the center of each plate to avoid the region where the coarse-grained density originating from the plate atoms is larger than or close to 0.5. If at some location, (y^*, z^*), the total coarse-grained density is below 0.5 at all x-values between $x_1 + b$ and $x_2 - b$, we assign $h_{\rm tube} = 1$, *i.e.*

$$\begin{aligned} h_{\rm tube} &= 1 \text{ if } \exists\, (y^*, z^*) \\ &\quad : \{\tilde{\rho}_{\rm total}(x, y^*, z^*) < 0.5\} \ \forall\, x \in (x_1 + b, x_2 - b) \\ &= 0 \ \text{ otherwise.} \end{aligned} \qquad \textbf{[S5]}$$

The cavity indicator function $h_{\rm cav}$ is similarly determined from $\tilde{\rho}_{\rm total}$. However, $h_{\rm cav}$ is equal to unity if the coarse-grained density is less than a half at some location between the plates, but not for all x-values between the plates. In other words,

$$\begin{aligned} h_{\rm cav} &= 1 \text{ if } \exists\, (x^*, y^*, z^*) \\ &\quad : \{\tilde{\rho}_{\rm total}(x^*, y^*, z^*) < 0.5\}\,,\ h_{\rm tube} = 0 \\ &= 0 \ \text{ otherwise.} \end{aligned} \qquad \textbf{[S6]}$$

Procedure for Calculating Unbiased Ensemble Averages

All umbrella sampling simulations performed in this work employ a biasing potential. Therefore, when performing ensemble averages of any observable, care must be exercised in accounting for the bias introduced by the potential. This is done using the WHAM/MBAR formalism [3, 4, 5], such that the unbiased ensemble average of any observable, $A(\overline{\mathbf{R}})$, which can be expressed as a function of the configuration vector, $\overline{\mathbf{R}}$, is given by

$$\left\langle A(\overline{\mathbf{R}}) \right\rangle = C^{-1} \sum_{j=1}^{K} \sum_{n=1}^{N_j} \frac{A(\overline{\mathbf{R}}_{j,n})}{\sum_{k=1}^{K} N_k e^{\beta F_k - \beta V_k(\overline{\mathbf{R}}_{j,n})}}, \qquad \textbf{[S7]}$$

where

$$C = \sum_{j=1}^{K} \sum_{n=1}^{N_j} \frac{1}{\sum_{k=1}^{K} N_k e^{\beta F_k - \beta V_k(\overline{\mathbf{R}}_{j,n})}}. \qquad \textbf{[S8]}$$

Here, F_k is the free energy of the kth biased ensemble, K is the number of biasing potentials or windows used, N_k is the number of samples in window k, V_k is the biasing potential for window k, and $\overline{\mathbf{R}}_{j,n}$ refers to configuration n in window j.

Equation S7 is used here to calculate the ensemble average of $h_{\rm tube}$, conditioned on the number of waters in confinement being N, according to

$$\left\langle h_{\rm tube}(\overline{\mathbf{R}}) \right\rangle_N = \frac{\left\langle h_{\rm tube}(\overline{\mathbf{R}}) \delta_{N,N(\overline{\mathbf{R}})} \right\rangle}{\left\langle \delta_{N,N(\overline{\mathbf{R}})} \right\rangle} \qquad \textbf{[S9]}$$

where $\delta_{N,N(\overline{\mathbf{R}}_{j,n})}$ is the Kronecker delta function. The ensemble average of $h_{\rm cav}$ as a function of N is calculated in an analogous manner by replacing $h_{\rm tube}(\overline{\mathbf{R}})$ with $h_{\rm cav}(\overline{\mathbf{R}})$ in Equation S9.

Average Shape of the Vapor Tube

The average shape of a vapor tube is identified by first taking the average of the coarse grained density, $\tilde{\rho}_{\rm tot}(x, y, z) \equiv \left\langle \tilde{\rho}_{\rm total}(x, y, z; \overline{\mathbf{R}}) \right\rangle$, over 5000 frames. Figure S3 displays the averaged density of the $d = 20$ Å system, with an average of 569 waters (top) and 474 waters (bottom) between the plates, obtained from biased simulations with $\tilde{N}^* = 570$ and $\kappa = 0.03$ kJ/mol and $\tilde{N}^* = 480$ and $\kappa = 0.03$ kJ/mol, respectively. From left to right in each row presents a front view, side view, and three-dimensional view of the averaged shape of the vapor tube. The three-dimensional rendering of the vapor tube is obtained as the iso-density surface $\tilde{\rho}_{\rm tot} = 0.5$, and this surface provides an accurate description of the average shape of the vapor tube. Additionally, the radii obtained directly from these isodensity surfaces, 1.03 nm and 1.30 nm, respectively for the top and bottom panels of Figure S3, are in reasonably good agreement with those obtained from the simple relation between r and N used in the main text (Equation S12), 1.22 nm and 1.45 nm, respectively. Note that the vapor tubes are cylindrical to a good approximation, in accord with macroscopic theory. However, further corrections to such theories could be obtained by taking into account finer details of the "hour-glass" shape of the vapor tubes. Because the precise shape of the vapor tubes depends on the details of the instantaneous interface calculation and the parameters employed, we do not attempt such corrections here.

Contact Angle Determination

The contact angle of the surface was determined by performing a 2 ns simulation of a cylindrical droplet containing 4142 water molecules. This cylindrical droplet was divided into five slabs, each 1 nm in width, and the density as a function of the radius y and the height z of each slab was computed. The droplet profile is then defined as the point where the density of the droplet is equal to half that of the bulk density.

The contact angle was then determined by fitting this droplet profile to a circle for $z > 0.7$ nm, as shown in Figure S4, where the fit function is given by

$$y = \sqrt{b^2 - (z - a)^2}. \qquad \textbf{[S10]}$$

Using this functional form, the contact angle, θ, can be obtained from

$$\left.\frac{dy}{dz}\right|_{z=0.7 \text{ nm}} = -\frac{(z - a)}{\left[b^2 - (z - a)^2\right]^{1/2}} = \frac{1}{\tan(\pi - \theta)}. \qquad \textbf{[S11]}$$

The contact angle was determined independently for each of the five slabs and averaged to yield a contact angle of $\theta = 120.2^\circ \pm 0.5^\circ$, or $\cos\theta = -0.503 \pm 0.008$.

Details of Vapor Basin Fits

Fitting used in the main text. In order to fit the simulated free energies to macroscopic theory, we consider the formation of a vapor tube of radius r, which depends on the number of waters, N, between the hydrophobic plates as

$$r \approx \sqrt{\left(\frac{N_{\rm liq} - N}{N_{\rm liq}}\right) \frac{L^2}{\pi}}. \qquad \textbf{[S12]}$$

Note that Equation S12 is an approximate expression; however, this simple approximation captures the salient features of vapor tube formation, as detailed below and in the main text. The free energy as a function of r as predicted by macroscopic theory is

$$\beta\Delta G(r) = 2\pi\beta\gamma\left[r^2\cos\theta + r\left(d_{\rm eff} + \frac{2\lambda}{\gamma}\right)\right] - 2\ln(1-\frac{2r}{L}), \quad \textbf{[S13]}$$

where γ is the liquid-vapor surface tension, θ is the contact angle (determined as described above), and λ is the line tension. The first term in Equation S13 is the free energy of vapor tube formation, $\Delta G_{\rm th}$, described in the main text, and the last term accounts for the translational entropy of the vapor tube. The effective distance between the plates, $d_{\rm eff}$, is obtained by subtracting a constant offset, ξ, from d, that is $d_{\rm eff} = d - \xi$. The x-intercept of a linear fit of the simulated d-dependence of $N_{\rm liq}$ is equal to ξ, as shown in Figure S5, so that a plot of $N_{\rm liq}$ vs $d_{\rm eff}$ passes through the origin. Here we find a value of the offset to be $\xi = 0.4964$ nm. The fits shown in Figure 4a of the main text were obtained by fitting the simulated free energies for $N < N_{\rm kink}$ and $r < L/2$ to the parameters, $\beta\gamma$ and λ/γ, using Equation S13; the fit parameters obtained are listed in Table 1.

Curvature Corrections. We also explored a number of other possible fits, the first of which includes curvature corrections to the surface tension using the Tolman length, δ, such that the curvature corrected surface tension is $\gamma(r) = \gamma(1-\delta/r)$. The fit equation then becomes

$$\beta\Delta G(r) = 2\pi\beta\gamma\left[r^2\cos\theta + r\left(d_{\rm eff} + \frac{2\lambda}{\gamma} - \delta\cos\theta\right) - \delta d_{\rm eff}\right] - 2\ln\left(1-\frac{2r}{L}\right). \quad \textbf{[S14]}$$

However, by referencing the simulated free energies for a given d-value to the free energy in the liquid basin, that is $\Delta G(N_{\rm liq}) = 0$, we force $\Delta G(r)$ to be 0 at $r = 0$. To be consistent with this convention, we neglect the constant term, $2\pi\gamma\delta d_{\rm eff}$ in Equation S14, and instead fit to

$$\beta\Delta G(r) = 2\pi\beta\gamma\left[r^2\cos\theta + r\left(d_{\rm eff} + \frac{2\lambda}{\gamma} - \delta\cos\theta\right)\right] - 2\ln\left(1-\frac{2r}{L}\right). \quad \textbf{[S15]}$$

From Equation S15, we see that the curvature correction δ acts in a manner analogous to the line tension λ, *i.e.* both are coefficients in the term linear in r. Therefore, we can simply relate the fit parameters in Equation S15 to those in Equation S13, according to

$$\frac{\lambda}{\gamma} = \frac{\lambda'}{\gamma'} + \frac{\delta}{2}\cos\theta, \quad \textbf{[S16]}$$

where the primed quantities indicate those obtained from Equation S13. The value of λ/γ obtained from Equation S15 can then be readily predicted with knowledge of the Tolman length. Recent estimates of this length for SPC/E water at 300 K yield $\delta \approx -0.1$ nm [6, 7]. Therefore, the value of λ/γ changes by ten to sixteen percent through the inclusion of the Tolman length in our fitting procedure.

Omission of Line Tension. To ascertain the importance of line tension, we attempt to fit the simulated free energies without including the term containing λ in our expression for the macroscopic theory, and instead using δ as a fit parameter according to

$$\beta\Delta G(r) = 2\pi\beta\gamma\left[r^2\cos\theta + r\left(d_{\rm eff} - \delta\cos\theta\right)\right] - 2\ln\left(1-\frac{2r}{L}\right). \quad \textbf{[S17]}$$

As one may anticipate from the above discussion, the data is fit equally well by Equation S17. However, this procedure yields unphysical estimates of the Tolman length, with $\delta \sim -1$ nm. Therefore, we can conclude that line tension is necessary to provide a physically accurate description of the vapor tube formation and growth that facilitates capillary evaporation between nanoscopic hydrophobic plates.

Liquid Basin Fits

In order to characterize the free energetics of isolated cavities, we fit the simulated free energies in the range, $N_{\rm kink} + 20 < N < N_{\rm liq} - 50$, to straight lines. We first fit the $d = 25$ Å free energy, and use the corresponding slope for all d-values. Intercepts are then obtained by fitting the data for each d-value separately. For $d \leq 16$ Å, data in the $N_{\rm kink} + 20 < N < N_{\rm liq} - 50$-range are insufficient to be fit reliably, so the fitting was not performed. The regions fit for each d-value are shown in Figure S6. In order to estimate errors, we divided the data into five blocks of equal length, and fit each block separately (similar block averaging analysis was performed for all quantities). Therefore, for each d, we show five data sets and five fits, although they are nearly indistinguishable.

From these fits, we can examine the behavior of $N_{\rm liq}(d) - N_{\rm int}(d)$, where $N_{\rm int}(d)$ is the x-intercept of the linear fit to the fat tails (for $d > 16$ Å). Both $N_{\rm liq}(d)$ and $N_{\rm int}(d)$ are roughly linear in d, see Figures S5 and S6, respectively. However, as shown in Figure S7, the quantity $N_{\rm liq} - N_{\rm int}$, which represents the distance in N from the liquid basin one must move to observe non-Gaussian tails in $\Delta G(N; d)$, or equivalently, to form isolated cavities, is largely insensitive to d.

Barrier Location and Height: Simulations vs Macroscopic Theory

In this section, we focus on the location as well as the height of the barrier, as predicted by macroscopic theory, and compare them with the corresponding simulated values. Macroscopic theory predicts a linear dependence of the location of the barrier, r^*, on d,

$$r^*(d) = -\frac{d_{\rm eff}}{2\cos\theta} - \frac{\lambda}{\gamma\cos\theta}, \quad \textbf{[S18]}$$

where we have neglected the logarithmic term in Equation S13. This behavior is captured by the data shown in Figure S8, where the r^*-values are obtained from the fits of the vapor tube free energetics to macroscopic theory. The slope of the fitted line corresponds to $\cos\theta = -0.547$, which is slightly larger in magnitude than that obtained from direct simulations. The ratio $\lambda/\gamma = -0.16$ nm obtained from the y-intercept of the linear fit lies in the same range as those predicted from fitting the free energies to Equation S13. Macroscopic theory also predicts $\Delta G(r^*; d)$ to be quadratic in d; this behavior is similarly captured as illustrated by fitting the data to a parabola (solid line).

In addition to the position and height of the maximum of the fits, we also include the position and the height of the free energy barrier obtained from the simulated free energy profiles, $r_{\rm max}(d)$ and $\Delta G(r_{\rm max}; d)$, respectively. For large d-values, we expect $r_{\rm max} \approx r^*$, however, this is not true at smaller plate separations because the critical vapor tube is in the metastable branch of the vapor tube free energy; for these d-values, the barrier corresponds to the kink in the free energy. Indeed, $r^* \neq r_{\rm max}$ at these separations, and the dependence of $r_{\rm max}$ on d can not be described by a straight line over the entire range of d. Similar behavior is observed in $\Delta G(r_{\rm max}; d)$, albeit to a lesser extent.

Data for All Systems Studied

For completeness, we include the free energies, their derivatives, $\langle h_{\mathrm{tube}}\rangle_N$, and $\langle h_{\mathrm{cav}}\rangle_N$, as well as fits to the vapor and liquid basins, for all d-values studied in Figures S9, S10, S11, S12, and S13 respectively. Additionally, we include the vapor basin fits and linear regions (where applicable) for all d-values in Figure S14.

Table 1: Parameters obtained from fitting the vapor tube portion of the free energy to Equation S13

d (Å)	$\beta\gamma$ (nm^{-2})	λ/γ (nm)
11	15.1	-0.150
12	15.4	-0.167
13	15.4	-0.177
14	15.4	-0.180
15	15.7	-0.180
16	15.0	-0.207
17	15.1	-0.208
18	14.6	-0.223
19	14.2	-0.230
20	13.7	-0.230
21	13.1	-0.243
22	13.3	-0.240
23	12.9	-0.234
24	12.5	-0.221
25	11.9	-0.216

1. Willard, A. P.; Chandler, D. Instantaneous Liquid Interfaces, J. Phys. Chem. B, 114, 1954–1958 (2010).
2. Lorensen, W. E.; Cline, H. E. Marching cubes: A high resolution 3D surface construction algorithm, Computer Graphics, 21, 163–169 (1987).
3. Ferrenberg, A. M.; Swendsen, R. H. Optimized Monte Carlo data analysis, Phys. Rev. Lett., 63, 1195–1198 (1989).
4. Tan, Z.; Gallichio, E.; Lapelosa, M.; Levy, R. M. Theory of binless multi-state free energy estimation with applications to protein-ligand binding, J. Chem. Phys., 136, 144102 (2012).
5. Shirts, M. R.; Chodera, J. D. Statistically optimal analysis of samples from multiple equilibrium states, J. Chem. Phys., 129, 124105 (2008).
6. Sedlmeier, F.; Netz, R. R. The spontaneous curvature of the water-hydrophobe interface, J. Chem. Phys., 137, 135102 (2012).
7. Vaikuntanathan, S.; Geissler, P. L. Putting water on a lattice: The importance of long wavelength density fluctuations in theories of hydrophobic and interfacial phenomena, Phys. Rev. Lett., 112, 020603 (2014).
8. Sharma, S.; Debenedetti, P. G. Evaporation rate of water in hydrophobic confinement Proc. Natl. Acad. Sci. U S A, 109, 4365–70 (2012).

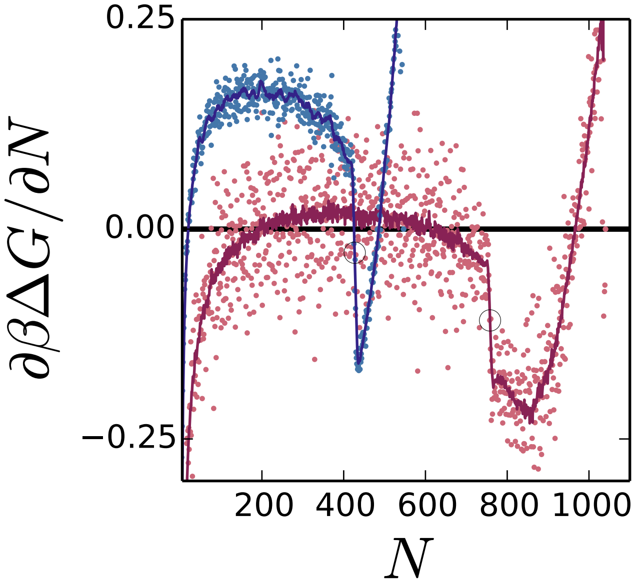

Figure S1: Derivatives of the unsmoothed (points) and smoothed (lines) free energies for $d = 14$ Å (blue) and $d = 23$ Å (red).

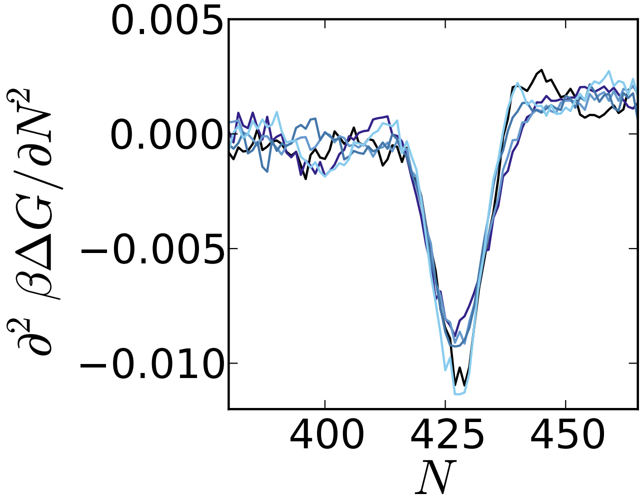

Figure S2: Second derivative of the free energy for $d = 14$ Å . Block averaging was used to obtain N_{kink} and its associated error bars; the derivatives of each of the five blocks are shown here. N_{kink} is the location of the minimum in $\partial^2\beta\Delta G/\partial N^2$.

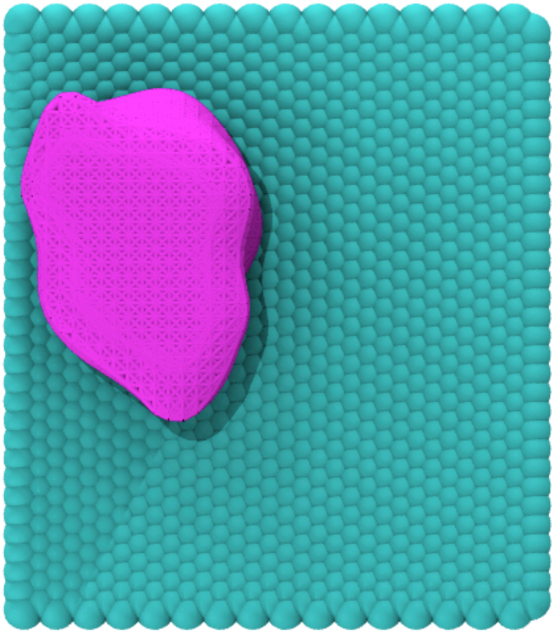

Movie S1: Movie illustrating a plate-spanning vapor tube in a biased simulation with $\tilde{N}^* = 650$ and $\kappa = 0.12$ kJ/mol, with $\left\langle \tilde{N} \right\rangle = 653$. Plate atoms are shown as spheres, while the purple mesh corresponds to the instantaneous interface enveloping the vapor region (water molecules have been omitted for clarity). The movie is shown from the direction perpendicular to the plane of the plates. The duration of the movie corresponds to 250 ps of simulation time.

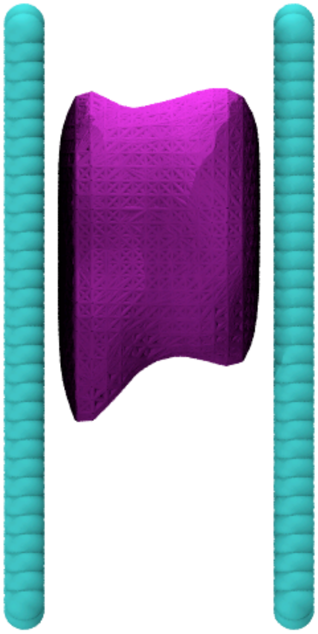

Movie S2: Movie illustrating a plate-spanning vapor tube in a biased simulation with $\tilde{N}^* = 650$ and $\kappa = 0.12$ kJ/mol, with $\left\langle \tilde{N} \right\rangle = 653$. Plate atoms are shown as spheres, while the purple mesh corresponds to the instantaneous interface enveloping the vapor region (water molecules have been omitted for clarity). The movie is shown from the direction parallel to the plane of the plates. The duration of the movie corresponds to 250 ps of simulation time.

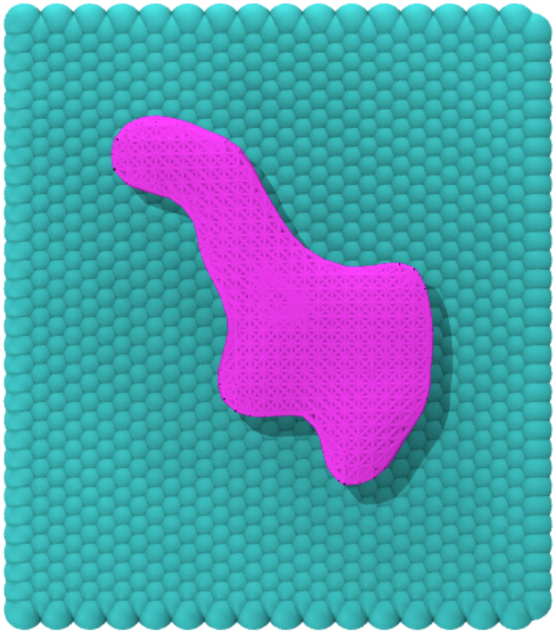

Movie S3: Movie illustrating vapor bubbles formed at the surface of a hydrophobic plate in a biased simulation with $\tilde{N}^* = 660$ and $\kappa = 0.12$ kJ/mol, with $\left\langle \tilde{N} \right\rangle = 668$. Plate atoms are shown as spheres, while the purple mesh corresponds to the instantaneous interface enveloping the vapor region (water molecules have been omitted for clarity).The movie is shown from the direction perpendicular to the plane of the plates. The duration of the movie corresponds to 250 ps of simulation time.

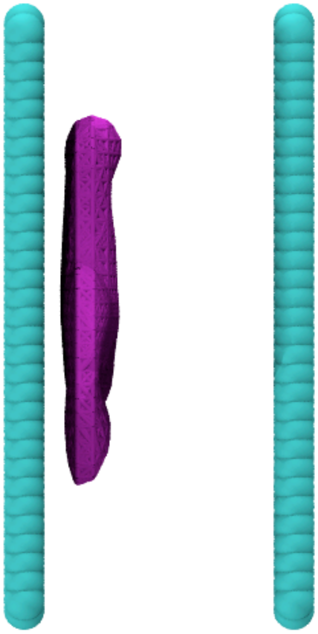

Movie S4: Movie illustrating vapor bubbles formed at the surface of a hydrophobic plate in a biased simulation with $\tilde{N}^* = 660$ and $\kappa = 0.12$ kJ/mol, with $\left\langle \tilde{N} \right\rangle = 668$. Plate atoms are shown as spheres, while the purple mesh corresponds to the instantaneous interface enveloping the vapor region (water molecules have been omitted for clarity).The movie is shown from the direction parallel to the plane of the plates. The duration of the movie corresponds to 250 ps of simulation time.

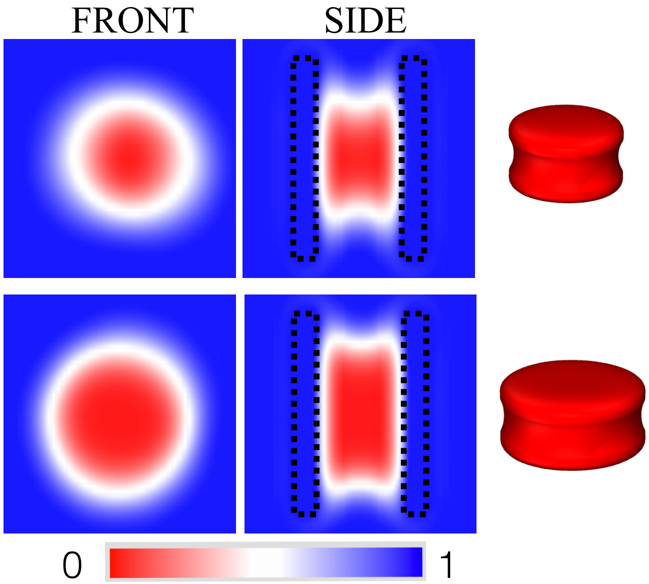

Figure S3: The average coarse-grained density, $\tilde{\rho}_{\rm tot}(x,y,z)$, for $d = 20$ Å , with an average of 569 waters (top) and 474 waters (bottom) between the plates. The top panel was obtained from a biased simulation with $\tilde{N}^* = 570$ and $\kappa = 0.03$ kJ/mol, and the bottom panel was obtained from a biased simulation with $\tilde{N}^* = 480$ and $\kappa = 0.03$ kJ/mol The rightmost panels depict three-dimensional renderings of the vapor tube shape at the iso-density surface $\tilde{\rho}_{\rm tot} = 0.5$

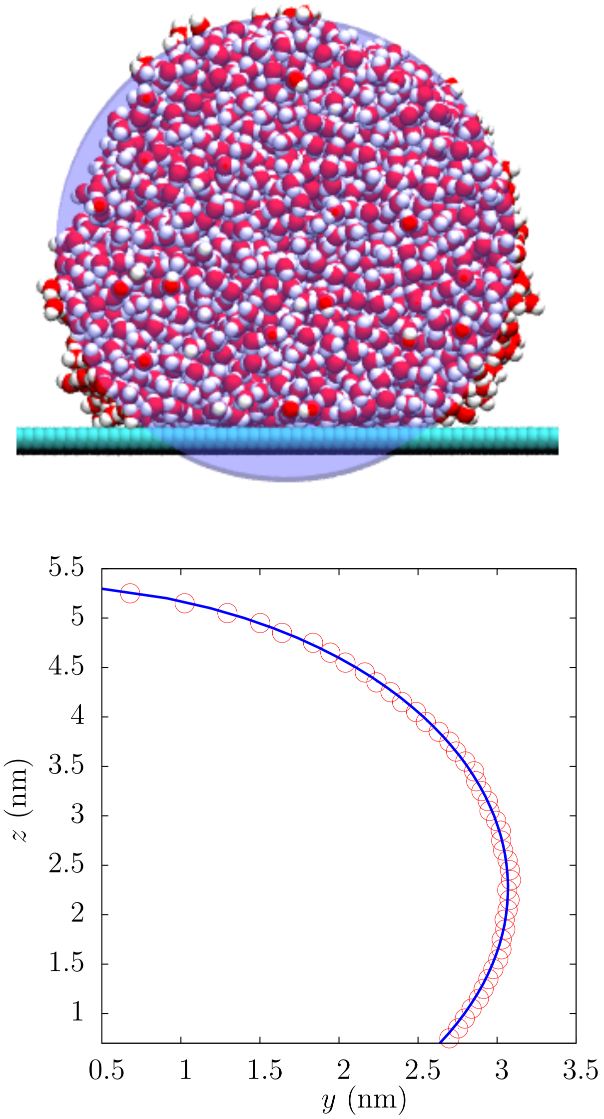

Figure S4: (top) Snapshot of the cylindrical droplet used to calculate the contact angle. (bottom) Fit of the average droplet profile (points) to Equation S10 (line).

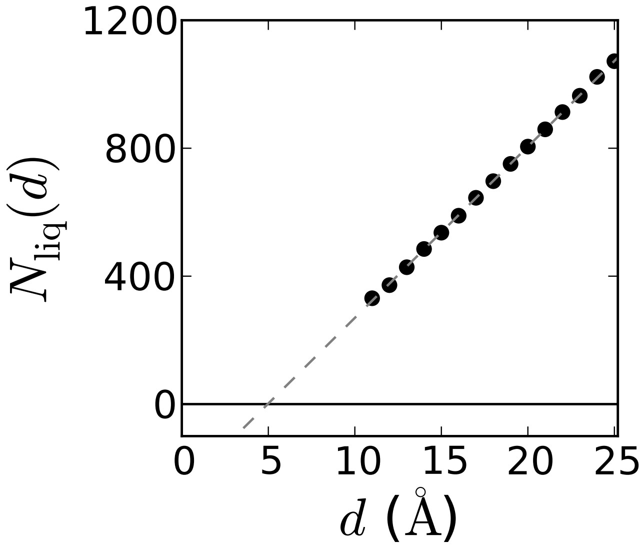

Figure S5: The number of water molecules between the plates in the liquid basin, N_{liq}, varies linearly with the distance between the plates, d, as measured between the centers of the atoms of the two plates. The effective distance between the plates, d_{eff}, is obtained subtracting from d the x-intercept, ξ, of a linear fit of $N_{\mathrm{liq}}(d)$; thus, $d_{\mathrm{eff}} = d - \xi$.

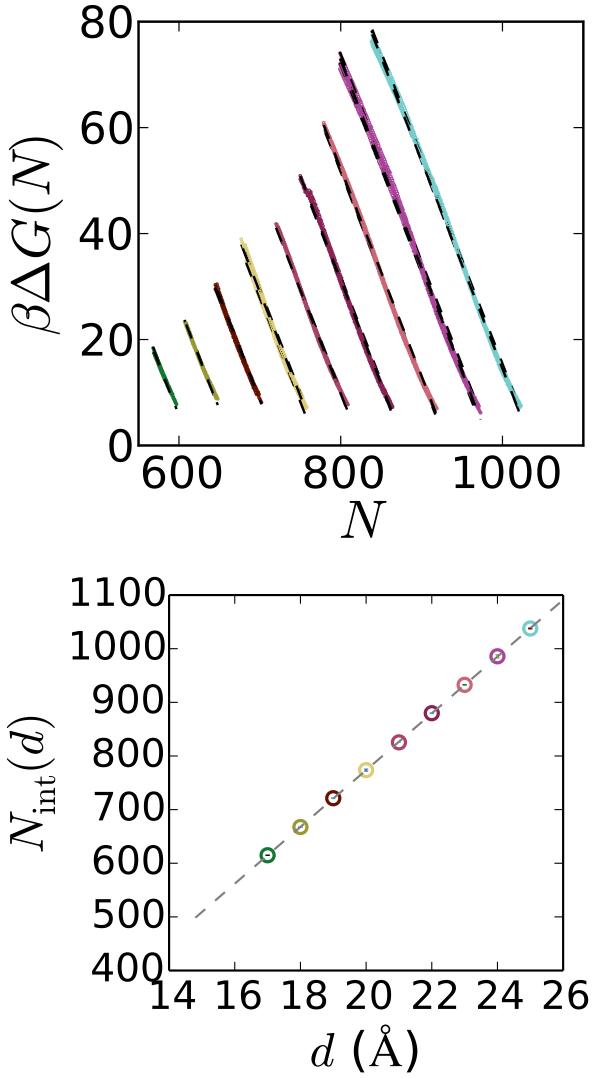

Figure S6: (top) Portions of the free energies that were linearly fit for $d > 16$ Å . Simulation data, split into five blocks for error estimation, is shown as colored data points. Linear fits are shown as black dashed lines. (bottom) The x-intercept, N_{int}, obtained from the linear fits, is plotted as a function of d.

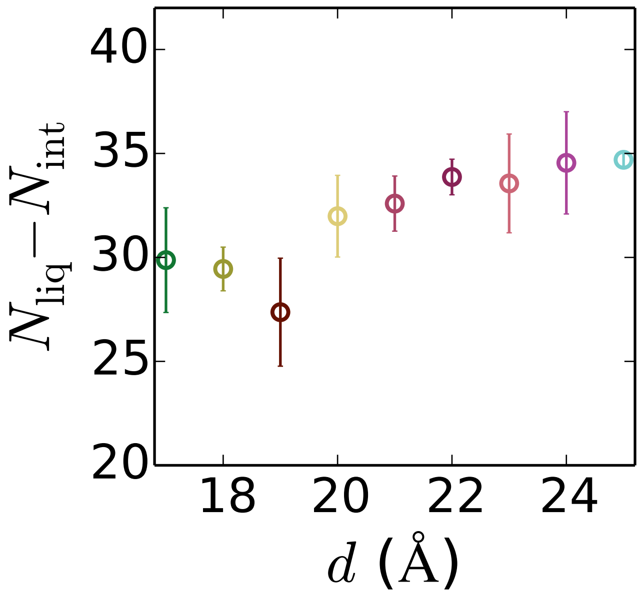

Figure S7: The number of waters needed to be removed from the liquid basin to encroach on the region of the fat tail, as measured by $N_{\mathrm{liq}} - N_{\mathrm{int}}$ for $d > 16$ Å . Error bars correspond to one standard deviation.

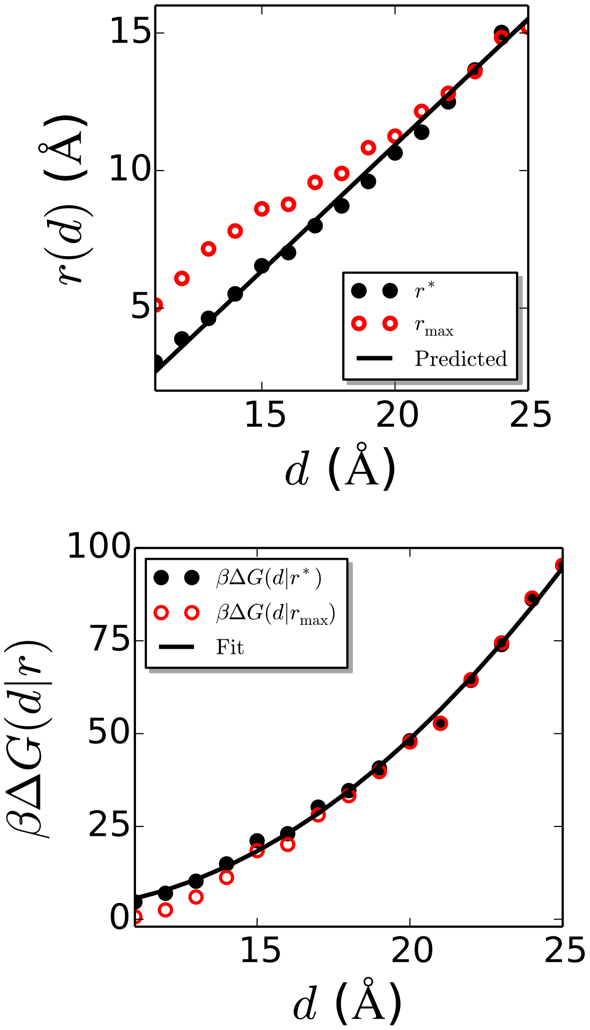

Figure S8: (top) Barrier position r^* and (bottom) barrier height $\beta\Delta G(r^*)$ of the fitted vapor tube free energies, are well-fit by linear and parabolic functions of the inter-plate separation, d, respectively, in agreement with macroscopic theory. In contrast, the simulated barrier position $r_{\max}$ and barrier height $\beta\Delta G(r_{\max})$ deviate from those functional forms.

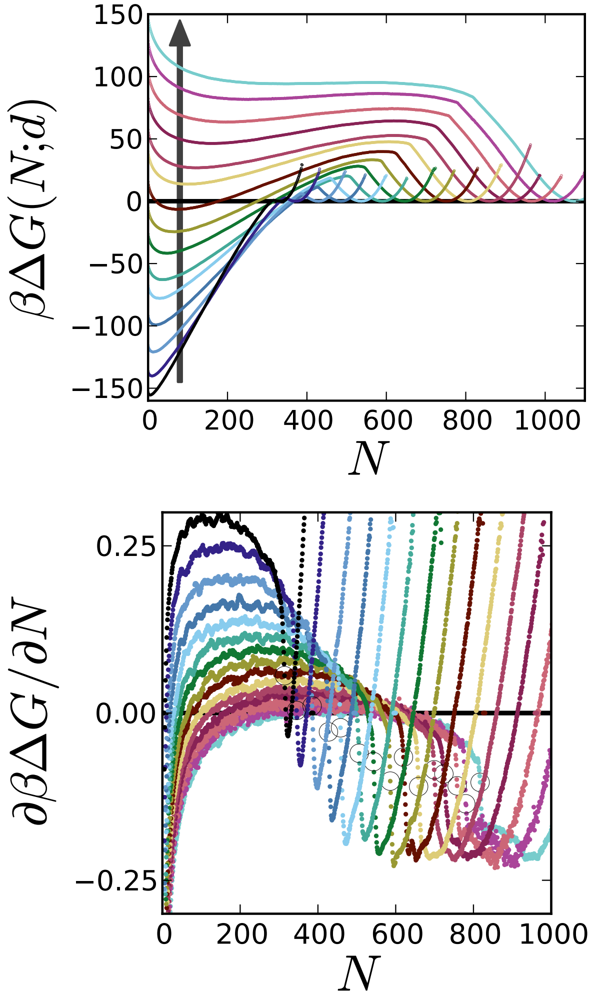

Figure S9: The dependence of (top) the free energies and (bottom) their smoothed derivatives on N for all d-values studied. Arrows point in the direction of increasing d, from $d = 11$ Å to $d = 25$ Å in increments of 1 Å .

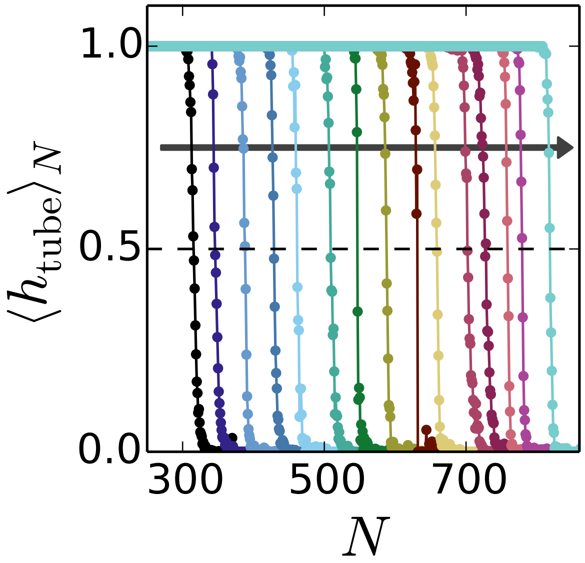

Figure S10: $\langle h_{\mathrm{tube}} \rangle_N$ for all d-values studied. Arrows point in the direction of increasing d, from $d = 11$ Å to $d = 25$ Å in increments of 1 Å .

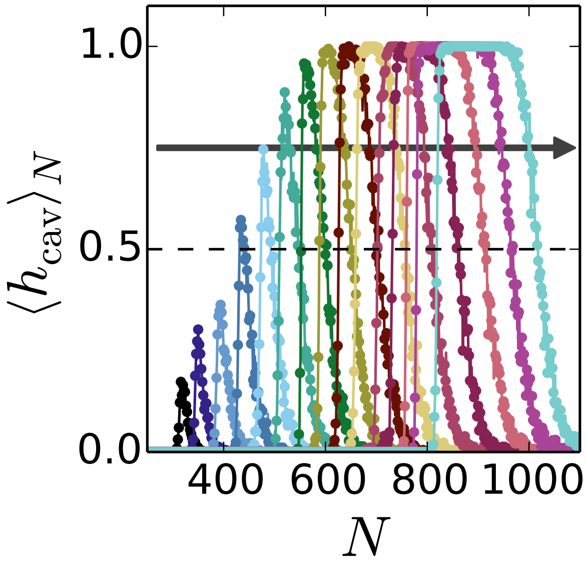

Figure S11: $\langle h_{\mathrm{cav}} \rangle_N$ for all d-values studied. Arrows point in the direction of increasing d, from $d = 11$ Å to $d = 25$ Å in increments of 1 Å .

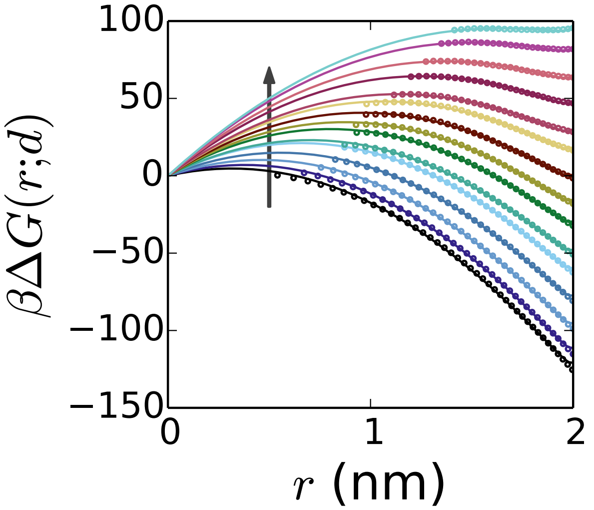

Figure S12: Free energies in the vapor basin ($N < N_{\text{kink}}$) and the corresponding fits to Equation S13. Simulation data is shown as points and the fits are shown as solid lines. The arrow indicates the direction of increasing d, from $d = 11$ Å to $d = 25$ Å in increments of 1 Å .

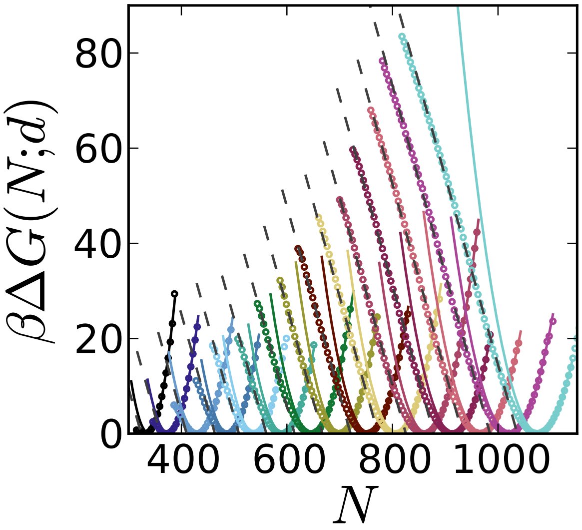

Figure S13: Free energies in the liquid basin ($N > N_{\text{kink}}$) and the corresponding parabolic (solid) and linear (dashed) fits to the right side of the minimum and to the fat tail regions, respectively.

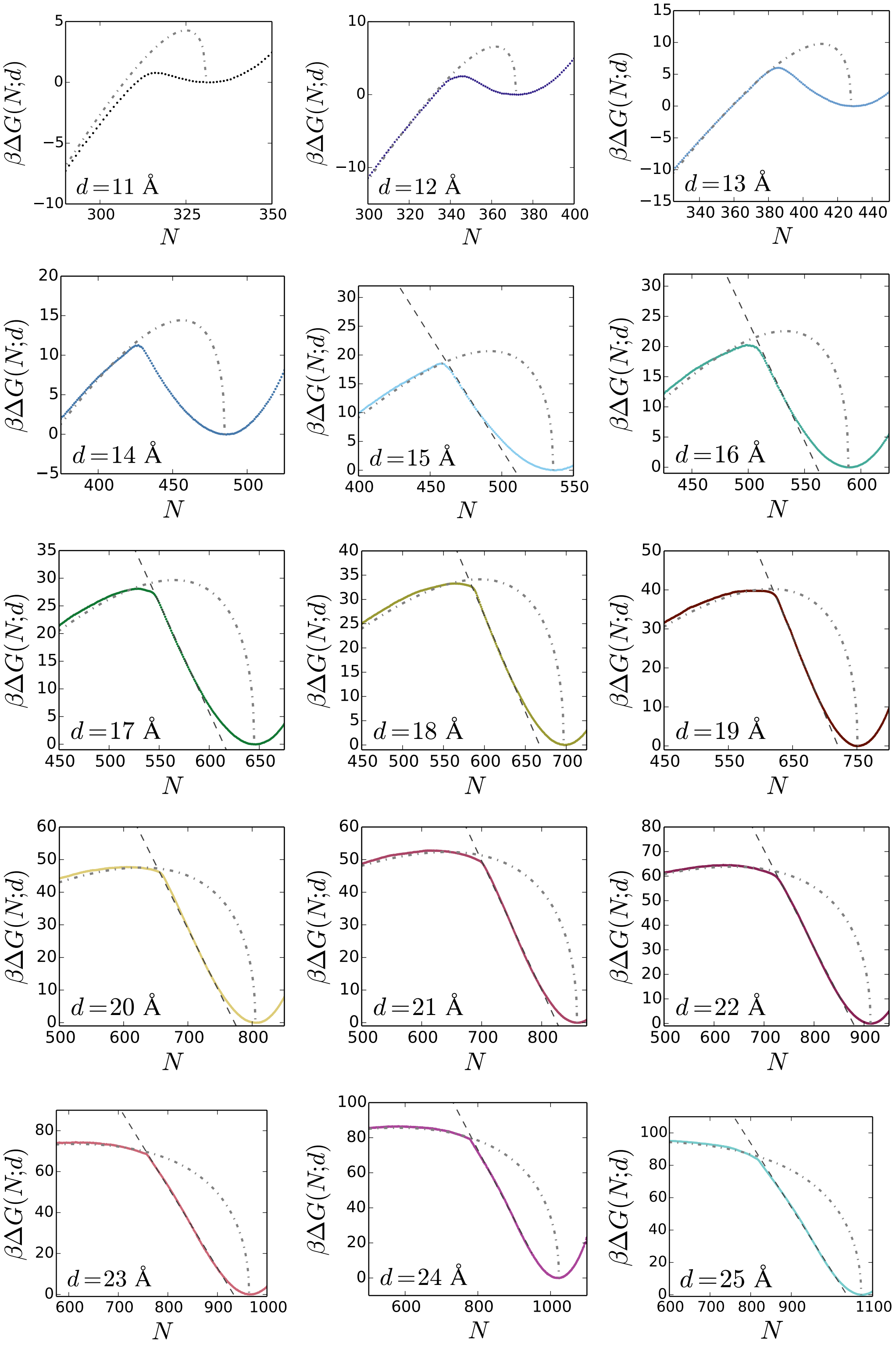

Figure S14: Vapor basin fits to Equation S13 (dot-dashed) and liquid basin linear fits (dashed) near N_{kink} for all d-values studied.